A fully-integrated wearable ultrasonic device for continuous blood pressure monitoring

Süleyman Yasin Peker[1,4], Yaşar Aykut Altuntop[1,4], Gürdeniz Neşer[2], Alp Toymus[2], Emine Bardakci[1], Emel Yılgör[3], İskender Yılgör[3], and Levent Beker[1,2,5,*]

[1]Department of Biomedical Sciences and Engineering, Koç University, Sariyer, Istanbul 34450, Turkey [2]Department of Mechanical Engineering, Koç University, Sariyer, Istanbul 34450, Turkey
[3]Department of Chemistry, Koç University, Sariyer, Istanbul 34450, Turkey
[4]These authors contributed equally
[5]Lead contact
*Correspondence: lbeker@ku.edu.tr

Table of Contents

Supplementary Note 1: Electrical characterization of the wearable ultrasound transducer.

The electrical impedance and phase of the 4.7-mm disc transducer were measured in the 1-3 MHz frequency range at these fabrication stages: (i) the bulk PZT, (ii) after applying a matching layer (75 wt% W filled D-230 epoxy-polyetheramine), and (iii) after applying a backing layer (75 wt% W filled D-2000 epoxy-polyetheramine). The electrical impedance and phase measurements at each fabrication step were performed in two configurations, namely in air and immersed in DI water. Conducting the impedance and phase measurements at different configurations enables us to assess the effect of acoustic loading. As presented in Supplementary Fig. 4, the electrical impedance magnitude (black) and phase (red) of the bulk disc PZT were measured in a 1-3 MHz frequency range in air (left) and in DI water (right). The measurements in air resulted in a resonance frequency (electrical impedance minimum) slightly above 2 MHz, followed by an anti-resonance frequency (electrical impedance peak) at 2.25 MHz. This steep phase transition is a characteristic of a transducer with a high-Q response. The impedance values measured were 23 Ohm at the resonance frequency and 1130 Ohm at the anti-resonance frequency. On the other hand, in the DI water-immersed measurements, these measurements were 56 Ohm at resonance frequency and 377 Ohm at anti-resonance, which shows that the anti-resonance peak was markedly reduced because of the acoustic loading. The impedance and phase measurements provide a baseline for the results after matching and backing layer coating.

Supplementary Fig. 5 shows the electrical impedance and phase measurements after the matching layer coating. There is a slight downward shift for both resonance and anti-resonance frequencies. The electrical impedance response was also damped after implementing the quarter-wavelength matching layer. The transducer's resonance frequency drops from 2 MHz to 1.85 MHz, and the anti-resonance frequency moves from 2.25 MHz to 2.12 MHz. The electrical impedance peaks also decreased to 367 Ohm in air and 250 Ohm in DI water. Adding a matching layer suppresses the anti-resonance impedance, while preserving the operating band around 2 MHz, which is complementary to the improved acoustic coupling and slightly reduced ringing compared to the bulk PZT.

As shown in Supplementary Fig. 6, the backing layer implementation further broadens and damps the electrical response relative to the matching layer added results. The resonance frequency occurs at 1.8 MHz with 86 Ohm, and the anti-resonance frequency at 2.21 MHz with a peak impedance of 200 Ohm. After the backing layer implementation, the lowest impedance contrast between the resonance and anti-resonance frequencies was obtained, which indicates improved damping and a reduced Q response. An ultrasound transducer with a broadened bandwidth centered around 2 MHz supports shorter pulses, which are crucial for a better acoustic performance.

Supplementary Note 2: Acoustic pressure field simulations of the WUT.

The acoustic pressure field response of the disc-shaped ultrasound transducers with radii of 1, 3, 4.7 and 7 mm were simulated using the Field II simulation program.[1,2] The Field II Simulation Program was used to model the disc-shaped ultrasound transducers as an ideal circular piston source (soft-baffled), driven by a three-cycle sinusoidal excitation with a Gaussian impulse response at 2 MHz with an amplitude of $10V_{pp}$. As a simulation environment, the soft-tissue characteristics were assumed such as the speed of sound was selected as 1540 m/s, frequency-dependent attenuation was selected as 0.5 dB/cm/MHz at 2 MHz with a baseline frequency-independent attenuation of 1.0 dB/cm.[3] The acoustic pressure fields were computed both in the longitudinal (x-z) plane and in the transverse (x-y) plane at fixed depth, which was selected as z = 3 cm to represent the typical depth of the common carotid artery.[4] The pressure field results were normalized to their peak values and plotted as relative amplitude (dB) to enable direct comparison of beam width and depth behavior across ultrasound transducer sizes.

As presented in both Supplementary Fig. 17 (longitudinal plane) and Supplementary Fig. 18 (transverse plane), the element radius directly affects the acoustic beam and operation depth. The ultrasound transducer with radius of 1.0 mm produces the lowest on-axis amplitude and a beam that is too wide at the target depth (~3 cm). On the other hand, the transducer with 7.0 mm radius exhibits an extended near field up to ~8 cm with amplitude fluctuations. So, the ideal ultrasound transducer should have a narrow acoustic beam profile in the typical target depth, which makes transducers with intermediate radii (3.0 and 4.7 mm) as potential candidates for the fabrication. Among these transducers, 4.7 mm radius produces the highest on-axis acoustic pressure with a compact main lobe around 3 cm. This transducer offers better performance to minor misalignment and tissue attenuation. That's why the transducer with 4.7 mm radius was selected for the fabrication.

Supplementary Note 3: Leach's equivalent circuit model for the simulation of the WUT.

The pulse-echo response of the wearable ultrasound transducer was simulated using Leach's equivalent circuit model. In this model, the backing layer, piezoelectric layer, matching layer, and propagating medium are represented as lossy transmission lines, while the reflective steel block is modeled as a resistor.[5–7] A sine wave input source with a 2 MHz operating frequency, $100V_{pp}$ input voltage, and a single-cycle burst is applied to simulate the pulse-echo experiments. The coaxial cable connecting the arbitrary waveform generator and the wearable ultrasound transducer is modeled as a 50 Ohm resistor. This setup provides an accurate simulation of the acoustic and electrical behavior of the WUT under experimental conditions.

The piezoelectric material parameters (f, C_0, h, and N) were calculated according to the following equations:

$$f = \frac{c_{pzt}}{2d} \tag{1}$$

$$C_0 = e^S * \frac{A}{d} \tag{2}$$

$$h = \frac{e^S}{\varepsilon_{33}} \tag{3}$$

$$N = h * C_0 \tag{4}$$

where f is the center frequency of the piezoelectric ceramic, c_{pzt} is the speed of sound in the piezoelectric ceramic, d is the thickness and A is the cross-sectional area of the piezoelectric ceramic. C_0 is the static capacitance of the piezoelectric ceramic. e^S is relative clamped dielectric constant. ε_{33} is the short circuit elastic constant. h is piezoelectric constant.

The propagation of sound waves was simulated by calculating the following lossy transmission line parameter equations:

$$L = A * \rho \tag{5}$$

$$C = \frac{1}{A * \rho * c^2} \tag{6}$$

$$R = 2\rho * c * A * \alpha \tag{7}$$

$$R_{pzt} = 2\pi * f * L * Q \tag{8}$$

where ρ, c, Q, α denote the density, speed of sound, quality factor and attenuation coefficient of the material. The lumped parameters L and C are the same for both piezoelectric ceramic and the acoustic media such as matching layer, backing layer and propagating medium. However, the resistance term R differs between the acoustic media and piezoelectric ceramic. Accordingly, above formulas were used to calculate resistance for the acoustic media, and for the piezoelectric ceramic.

Supplementary Note 4: Power management module electronics hardware design.

The power management module was powered by a 3.7V Li-Po battery, and this module generates five different regulated rails: 3.3V, 5V, -5V, 32V, and 1.5V.

In order to generate a 3.3V, the NCV8187 low dropout (LDO) linear voltage regulator (Onsemi Semiconductor Components Industries, LLC) was used. This 1.2A, LDO regulator with a fixed 3.3V output voltage is a stable device with a very low quiescent current (typically 30μA). For input decoupling, a 1μF ceramic X5R capacitor was connected between the input and ground pin of the device. This capacitor provides a low impedance path to unwanted AC signals and noise. Likewise, a 10μF output decoupling capacitor was used between this regulator's output and ground pins to obtain a stable regulated output.

A 1.8A peak switch-current limit boost converter with a fixed 5V output voltage (TPS61322, Texas Instruments Inc.) was used to generate the 5V regulated output rail from an input voltage of 3.7V. This boost converter has a very low quiescent current (6.5μA) and delivers more than 90% efficiency under typical load conditions. A 2.2μH was used so that the boost converter works in continuous operation mode up to 500 mA maximum load. The high switching frequency of the boost converter requires a high-speed rectifying switch for efficiency. A Schottky diode was selected with a peak current rating higher than the inductor's peak current. Since the diode was soldered on the PCB, a snubber circuit consisting of a 5.1 Ohm resistor and a 120pF capacitor was implemented. Decoupling capacitors were implemented for effective output voltage filtering.

A fixed -5V inverting DC/DC converter with 200mA output current (TPS6735ID, Texas Instruments Inc.) was employed to generate a -5V voltage rail from the 5V rail of the boost converter. To suppress the noise and provide stability, bypass capacitors were used and placed close to the inverting converter. The ground and input pins of the integrated circuit (IC) were bypassed directly with a 1μF capacitor to enable robust and noise-reduced operation. A 100nF soft start capacitor provided the switch current limit of the inverting converter during the power-up. Moreover, a 10μH inductor with a 300mA current, higher than the peak switch current of the inverting converter, was used for proper operation. A Schottky diode with a maximum continuous current rating higher than 200 mA was implemented for rectification.

The 32V high-voltage pulse rail was regulated using a 1.5A peak boost switching converter (MC33063A, Texas Instruments Inc.) which contains a comparator, an oscillator, a Pulse Width Modulation (PWM) controller with active current limiting, a driver and a high-current output switch. This converter was configured to operate as a step-up converter. The 3.7V rail was supplied to the IC as an input voltage.

A 100μF, 50V electrolytic capacitor was used at the output to reduce the output ripple and 100μF input decoupling capacitor was employed at the input. A 180μH, 0.51A inductor was added with a 40V Schottky diode for boost converter operation. The 32V regulated output voltage rail was adjusted using the R_2 = 24.6 KOhm and R_1 = 1 KOhm according to the following equation:

$$V_{out} = 1.25 * \left(1 + \frac{R_2}{R_1}\right) \quad (9)$$

where R_2 is the resistor between the Schottky diode and comparator, and R_1 is the resistor between the comparator and ground.

The reference voltage used for the differential amplifier unit was generated by the voltage divider and buffer unit which contains a CMOS operational amplifier (op-amp) with shutdown (OPA357, Texas Instruments Inc.). This operational amplifier is low-noise and low quiescent current (4.9mA)

with a 250 MHz unit-gain bandwidth used as a buffer to isolate and stabilize the 1.5V output rail. To adjust the DC offset voltage, a 3.3V input was supplied to the voltage divider circuit with $R_1 =$ 680 Ohm and $R_2 =$ 560 Ohm according to the following equation:

$$V_{Ref} = V_{in} * \left(\frac{R_2}{R_1 + R_2}\right) \tag{10}$$

where R_1 is the resistor between the input voltage and non-inverting terminal of the operational amplifier, and R_2 is the resistor between the non-inverting terminal of the operational amplifier and ground.

Supplementary Note 5: Frontend module electronics hardware design.

The frontend module of the fully integrated wearable ultrasound device performs the timing and sequencing of the sub-units, pulse generation, US transducer excitation and echo receiving, signal conditioning, A/D conversion, and wireless data transfer. This miniaturized device has dimensions of 35 mm x 40 mm. The frontend is powered by the regulated voltage rails, which were generated by the power management module. The main blocks of this module are an MCU/ADC unit which controls pulsing and data acquisition, a HV pulser unit with a T/R switch which generates the high-voltage pulses to drive the wearable ultrasound transducer and receives the backscattered echo signals, a differential amplifier with DC offset unit to avoid echo clipping during the amplification, a low-pass filter unit to suppress unwanted high frequency noise, an IMU unit for motion and acceleration monitoring, and a Wi-Fi unit for wireless data transfer to the host computer.

The main processing and data acquisition unit is an ultra-low-power ARM Cortex-M4 MCU (STM32L476RG, STMicroelectronics Inc.) running up to 80 MHz. Two 8-bit Successive-Approximation Register (SAR) ADCs in interleaved mode which operate at a sampling rate of ~15 MS/s were utilized to drive the wearable ultrasound transducer with a center frequency of 2 MHz. This sampling rate is Nyquist rate-compliant with an additional safety margin. The MCU is powered from the regulated 3.3V rails, and to suppress high-frequency power supply noise, decoupling capacitors and a chip ferrite bead were employed. To reduce the size of the design, the internal 16 MHz oscillator of the MCU was used (no external oscillators). A status Light Emitting Diode (LED) was added to monitor the MCU's operation.

In order to drive the ultrasound transducer, a high-voltage pulser (MAX14808, Analog Devices Inc./Maxim Integrated) with an integrated T/R switch was used. There are eight independent channels with T/R switches, and each channel supports three-level pulses controlled by the DINN and DINP logic inputs, while the amplitude of the generated pulses was set by the HV rail. These eight independent channels with a T/R switch show the design flexibility of our fully integrated system to drive array transducers up to 8 elements. To design this HV pulser unit, small-valued decoupling capacitors were used to suppress the high-frequency noise, and high-valued capacitors were used to suppress noise due to the power line. The HV pulser was driven from a 3.3V logic rail and 5V, and -5V low-voltage (LV) rails, with a programmable 32V high-voltage rail. The amplitude of the pulses is tunable by adjusting the HV rail.

A-first order passive RC low-pass filter was implemented after the amplification to attenuate the high-frequency noise and switching transients while maintaining the 2 MHz echo signals. The operating frequency of the wearable ultrasound transducer is 2 MHz, and with a safety margin, the RC low-pass filter with a -3 dB cutoff frequency at 3.93 MHz was designed according to Equation 4.3. A 2.7 Kohm resistor and a 15pF capacitor were employed to design the low-pass filter. This low-pass filter provides a passband with a minimal distortion up to the cutoff frequency as presented in magnitude and phase plots (Supplementary Fig. 12).

$$f_c = \frac{1}{2\pi RC} \tag{11}$$

where f_c is the -3 dB cutoff frequency of the filter, R and C are the resistor and capacitors of the RC low-pass filter.

The inertial measurement unit includes an ultra-low-power three-axis accelerometer (LIS3DSH, STMicroelectronics Inc.) to track the motion and acceleration information. This unit is powered by the regulated 3.3V voltage rail and communicates with the MCU over Inter-Integrated Circuit (I^2C) protocol. This IC was configured for low-power operation, and the acceleration data were sampled and time-stamped in parallel with the ultrasound signals. It also includes an on-board temperature sensor, which was used as a safety measurement to monitor and track the temperature of the fully integrated system.

A 2.4 GHz Wi-Fi System on a Chip (SoC) with an on-board PCB antenna (ESP32-S3-WROOM-1-N8R8, Espressif Systems) was used for wireless communications. This Wi-Fi unit includes a dedicated 3.3V LDO linear voltage regulator (NCV8187, Onsemi Semiconductor Components Industries, LLC) to supply a stable voltage rail to the ESP32. The conditioned and digitized ultrasound signals were streamed over Serial Peripheral Interface (SPI) and wirelessly transmitted to the host computer.

Supplementary Note 6: Motion mode ultrasound imaging algorithm.

Motion Mode is a form of US imaging that generates a depth/time image by repeatedly transmitting the A-mode US signals and stacking the received signals column-wise.[8] Using the M-mode US images, moving targets such as wrist and finger motion, arterial wall movement, and abdominal muscle thickness can be measured.[9–11] The simplicity of the M-mode image comes from the need for a single piezoelectric element, compared to the Brightness Mode (B-mode) which requires multiple piezoelectric elements and complex beamforming electronics. In order to facilitate the advantage of the simplicity of a single-element ultrasound transducer, an M-mode US image generation algorithm was developed from the A-mode US signals, which enables tracking the pulsatile movement of the carotid arteries and timing information of each cardiac cycle can be acquired.

In order to generate M-mode images from the A-mode signals, firstly, the analytic signal $s_a(t)$ was computed by Hilbert transform. Then, the upper signal envelopes were calculated by taking the absolute value of the analytic signal as described in the following equation:

$$A(t) = |s_a(t)| \tag{12}$$

where $s_a(t)$ is the analytic signal, and $A(t)$ is the upper envelope (magnitude) of the signal.

The calculated envelopes were converted to a decibel image by log-compression for dynamic-range matching. By log-compression, the speckles were compressed, and bright regions corresponding to the arterial wall echoes can be seen with an improved contrast.

$$L(t) = 20 * log_{10}(A(t) + \varepsilon) \tag{13}$$

where $L(t)$ is the compressed A-mode line, and ε is the safety constant to prevent calculating the $\log_{10}(0)$ and setting the lowest displayable level.

Each 1D compressed A-mode line was stacked to generate a 2D matrix M (time, frame). The x-axis of the matrix M is the time axis, and the y-axis of the matrix M is the time-of-flight, which is converted into depth according to the following equation:

$$z = \frac{c}{2} * t \tag{14}$$

where z is the depth, c is the speed of sound, and t is the time-of-flight.

The impulsive noise was suppressed using a 2D median filter without blurring the arterial walls, a 2D median filter were. A bilateral filter was implemented to further denoise the image. In this way, the high-contrast edges were preserved while filtering the noise. The filtered image was normalized using a percentile clipping to improve the visibility of the pulsatile arterial walls and remove the regions out of interest. Additionally, an unsharp mask was applied to improve the

details of the arterial walls. Cubic interpolation along the time and depth axes was used for smoothing and reducing pixelation.

The developed M-mode US imaging algorithm was used to monitor the carotid artery. During each cardiac cycle, the carotid artery expands and contracts, corresponding to the systolic and diastolic phases of blood pressure. This dynamic motion was captured in the grayscale M-mode image, which visualizes the periodic distension of the anterior and posterior artery walls.

Supplementary Note 7: Blood pressure measurement methodology.

Blood pressure measurements were derived from the shifts of the anterior and posterior walls of the common carotid artery. As the arterial walls move during systolic and diastolic phases, the diameter of the CCA changes, enabling the calculation of blood pressure values based on these dynamic diameter variations.

The ultrasound transducer was positioned on the neck of the subject, targeting the CCA. The backscattered echo signals from the anterior and posterior walls of the artery were captured at a high sampling rate of 15 MS/s. The acquired ultrasound signals were processed using the signal processing algorithm to determine the time-of-flight values for the anterior and posterior wall reflections. These time-of-flight values were then utilized to calculate the dynamic diameter of the CCA using the following equation:

$$d(t) = \frac{t_2 - t_1}{2} * c \tag{15}$$

where $d(t)$ represents the CCA diameter as a function of time, t_1 and t_2 represent the arrival time of the anterior and posterior walls respectively, and c which represents the speed of sound through tissues, set at 1540 m/s, the commonly accepted average speed of sound in soft tissues.

The cross-sectional area of the CCA was then computed from the dynamic diameter values using:

$$A(t) = \frac{\pi d^2(t)}{4} \tag{16}$$

where A(t) represents the area of the CCA as a function of time, and $d(t)$ represents the artery diameter as a function of time.

To calculate the arterial compliance, the alpha coefficient α was determined using the following formula:

$$\alpha = \frac{A_d * ln\left(\frac{p_s}{p_d}\right)}{A_s - A_d} \tag{17}$$

where A_s and A_d denote the systolic and diastolic cross-sectional areas of the CCA, respectively, and p_s and p_d represent the systolic and diastolic blood pressure measurements obtained from the cuff.

Finally, the blood pressure waveform, $p(t)$, was estimated using the following equation:

$$p(t) = p_d + e^{\alpha\left(\frac{A(t)}{A_d}-1\right)} \quad (18)$$

This methodology enables accurate calculation of blood pressure based on dynamic arterial wall movements, providing a non-invasive approach to continuous blood pressure monitoring.

Supplementary Note 8: Signal processing algorithm for blood pressure monitoring.

The received US signals are processed as presented in Supplementary Fig. 16 to track the pulsatile movement of the arterial walls. Firstly, the raw US signals are acquired frame-by-frame, and a band-pass filter is applied to each US signal frame to suppress the high and low frequency noises outside of the bandwidth. The band-pass filter was configured with lower- and upper- cutoff frequencies of 1 MHz and 4 MHz. The Hilbert transform calculates the upper envelope of the acquired echo signals. Then, the peak points corresponding to the anterior and posterior walls are detected. These signal peaks segment the arterial walls' region of interest (ROI). For each frame, ROIs are segmented, and these segments are correlated with their following segments to calculate the lag in the signal in positive and negative directions. According to these lagging, the distensions of the anterior and posterior walls are measured in time. Tracking the maximum value in the correlation result allows monitoring the anterior and posterior wall movement.

Supplementary Note 9: Fabrication of the wearable ultrasound transducer.

The wearable ultrasound transducer consists of a disc-shaped PZT element, a casing, acoustically optimized matching and backing layers, a PDMS encapsulation layer, wires and silicone fillings as presented in Supplementary Fig. 19. The disc-shaped PZT-5H piezoelectric ceramic (APC-850, American Piezo International Ltd.) with a radius of 4.7 mm and a thickness of 1 mm was used for the fabrication of the WUT. The disc PZT employs a wrap-around electrode configuration, which enables both electrical pads of the transducers to be accessed from a single side of the transducer.

The designed mechanical casing of the US transducer was 3D-printed using clear resin. The top and oblique views of the fabricated casing are shown in Supplementary Fig. 20a,b. The housing includes four internal seating pads spaced at 90° around the inner walls to support the disc PZT inside of the casing. A narrow wiring slit located in the side wall was designed to provide a pathway to the transducer wires.

The disc PZT was seated inside of the casing and oriented so that the wrap-around pad aligned with the wiring slit, allowing safe routing of the transducer wirings to their pads (Supplementary Fig. 20c,d.

After placement of the disc PZT, the 75 wt% W-filled D-230 epoxy-polyetheramine matching layer was applied to the radiating surface. The matching layer composite was prepared, mixed and degassed, then dispensed to the PZT surface according to the quarter-wavelength thickness at 2 MHz and cured at 80°C for 4 hours.

After curing the matching layer, the radiating surface of the device was encapsulated to provide a biocompatible, and electrically insulating package. PDMS (Sylgard 184, 10:1 base to curing agent ratio) was used for the encapsulation layer, and prepared by mixing with the predefined ratio, then vacuum-degassed and drop-cast over the matching layer. The coating was leveled and cured at 100°C for 35 minutes. The resulting PDMS encapsulation forms a smooth skin-contact surface as shown in Supplementary Fig. 20e,f.

The electrical connection was made using a conductive silver-epoxy (8331D, MG Chemicals) as presented in Supplementary Fig. 20g,h. The two-part conductive epoxy was mixed with 1.1:1 weight ratio and applied to the pads. Then, the wires were inserted from the narrow wire slit, and seated into the silver-epoxy, and remained stationary during the curing stage. The silver-epoxy was cured at 65°C degrees for 10 minutes. After curing, the electrical connections and resistance values were measured to validate the bonding of the wires to their corresponding pads.

After completing the wire bonding, the backing layer (75 wt% W-filled D-2000 epoxy-polyetheramine) was prepared. The composite was thoroughly mixed and degassed. The mixture was dispensed onto the back of the disc PZT inside the casing, and filled to target thickness of 3 mm. The poured backing layer was leveled and cured at 80°C for 4 hours (Supplementary Fig. 20i,j). The fabricated backing layer provides mechanical support, suppresses unwanted signals, and reduces ringing effect, which results in shorter pulses and broader bandwidth.

Supplementary Note 10: Power consumption and battery life of the FIWUS.

The fully integrated wearable ultrasound system is powered by a small-sized 3.7V and 150mAh Li-Po battery to be used in continuous blood pressure monitoring and health monitoring applications. The average current consumption of the components in the system is presented in Supplementary Table 1. The total average current consumption is 163.5mA with a 3.7V input. Thus, the average power consumption of the fully integrated wearable ultrasound system is ~605 mW. So, this system can continuously operate for ~1h. The power consumption of the system can be further optimized by configuring the device to operate periodically and by increasing the size of the battery up to ~4-5h.

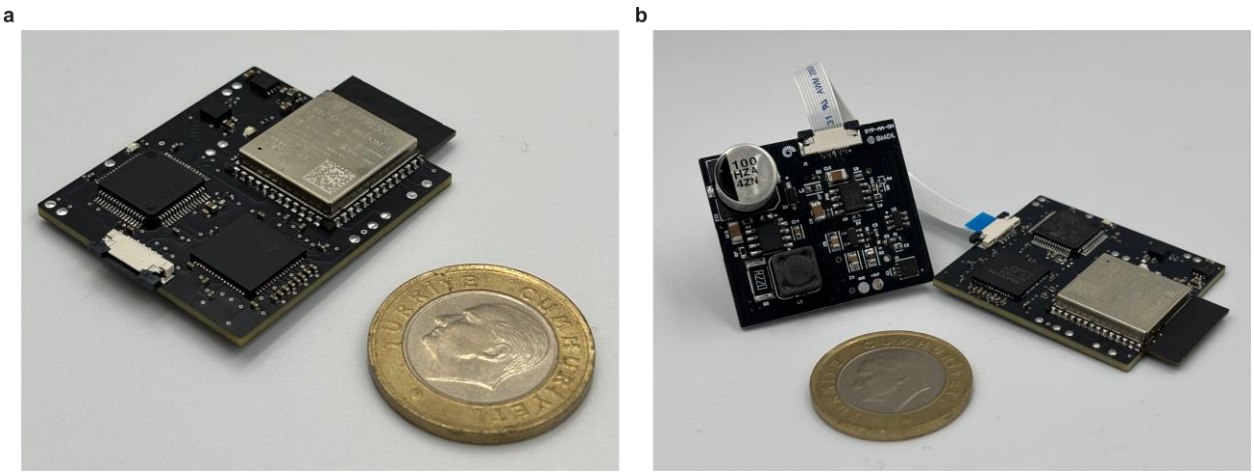

Supplementary Fig. 1: Miniaturized design of the FIWUS. a, Photograph of the compact frontend module with wireless communication and signal processing circuitry next to a 1 Turkish Lira coin for scale. **b,** Photograph of the assembled fully integrated wearable ultrasound system including the power management and frontend modules. A 1 Turkish Lira coin is shown for scale.

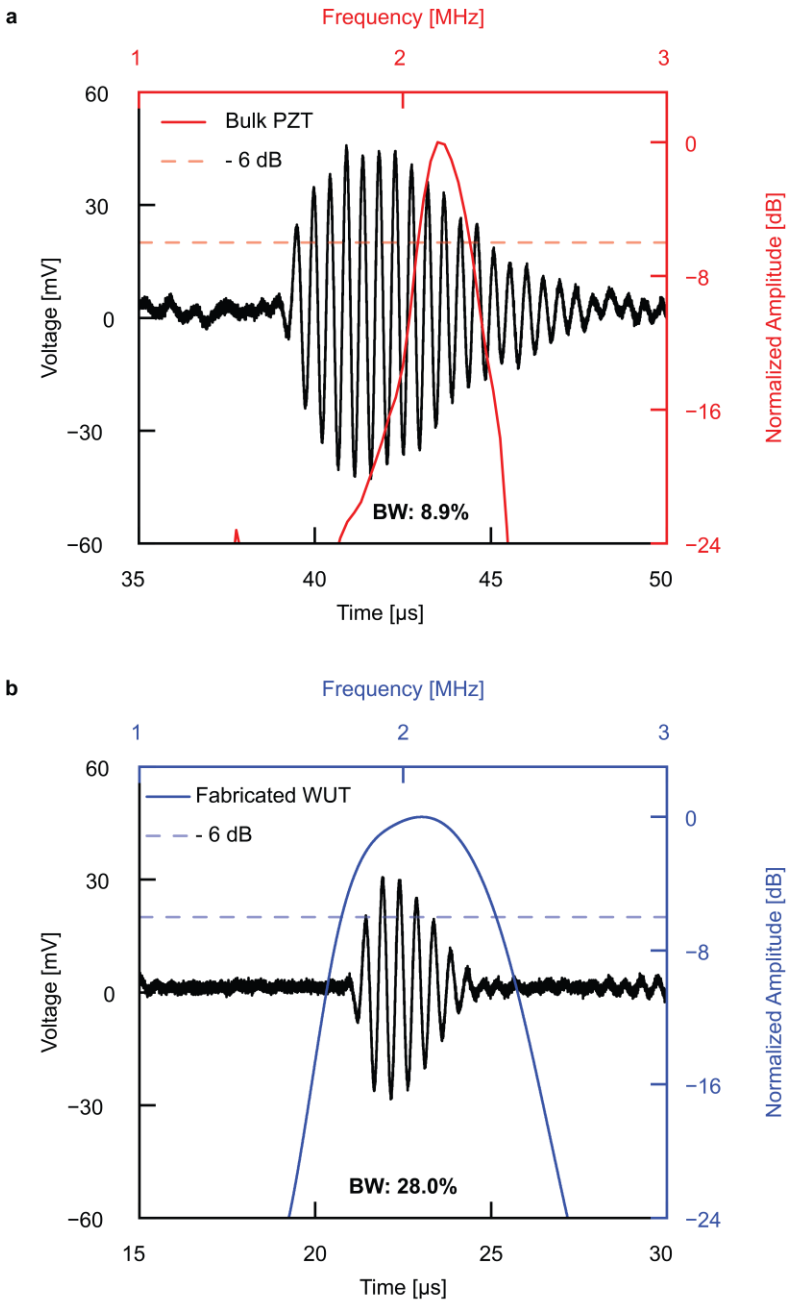

Supplementary Fig. 2: Pulse-echo response and corresponding normalized FFT spectrum of the disc-shaped transducer with -6 dB reference indicated. a, Pulse-echo response of the bulk PZT showing an 8.9 % fractional bandwidth. **b,** Pulse-echo response of the fabricated WUT showing a 28.0 % fractional bandwidth.

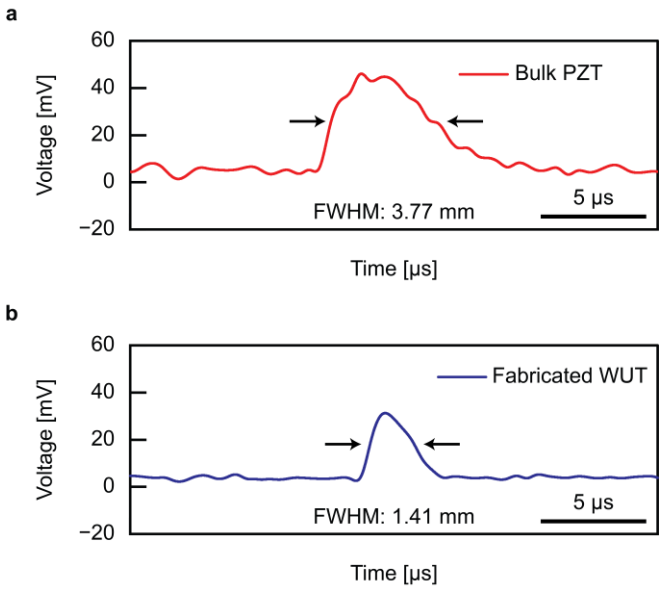

Supplementary Fig. 3: Time-domain upper envelopes of the bulk PZT and fabricated WUT to compute the FWHM. a, Upper envelope of the bulk PZT showing a 3.77 mm axial FWHM. **b,** Upper envelope of the fabricated WUT showing a 1.41 mm axial FWHM.

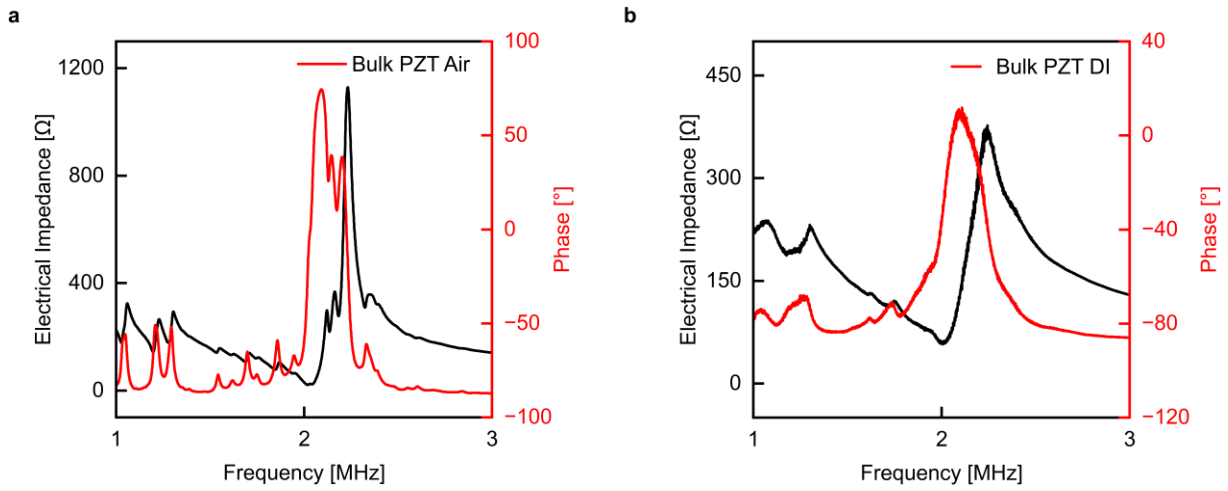

Supplementary Fig. 4: Electrical impedance magnitude and phase response of the bulk piezoelectric (PZT) ceramic. a, b, Frequency sweep results of the bulk PZT from 1 MHz to 3 MHz in air **(a)** and in DI water **(b)**.

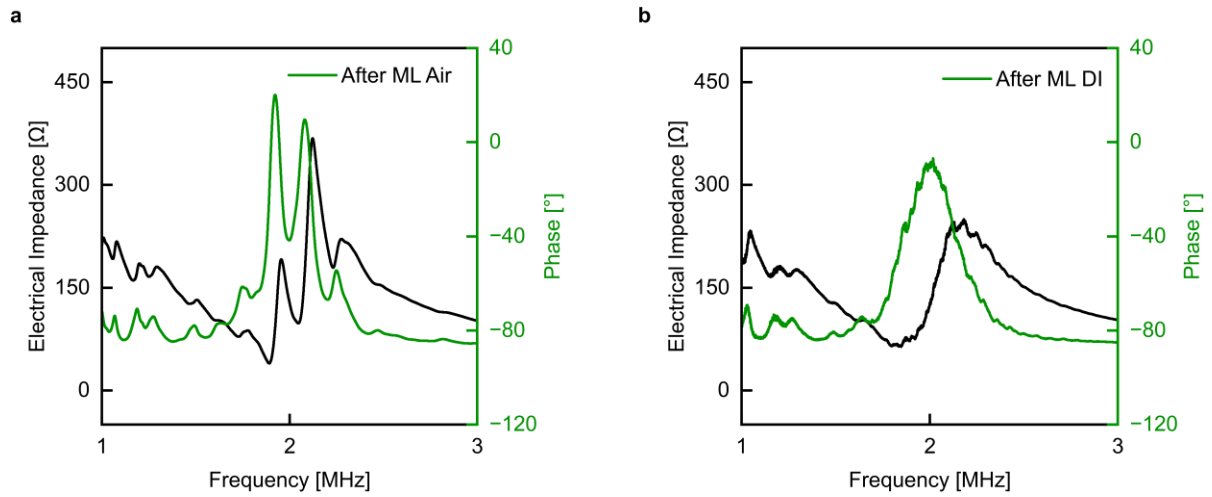

Supplementary Fig. 5: Electrical impedance magnitude and phase response of the WUT after matching layer (ML) coating. a, b, Frequency sweep results of the ML-coated wearable ultrasound transducer from 1 MHz to 3 MHz in air **(a)** and in DI water **(b)**.

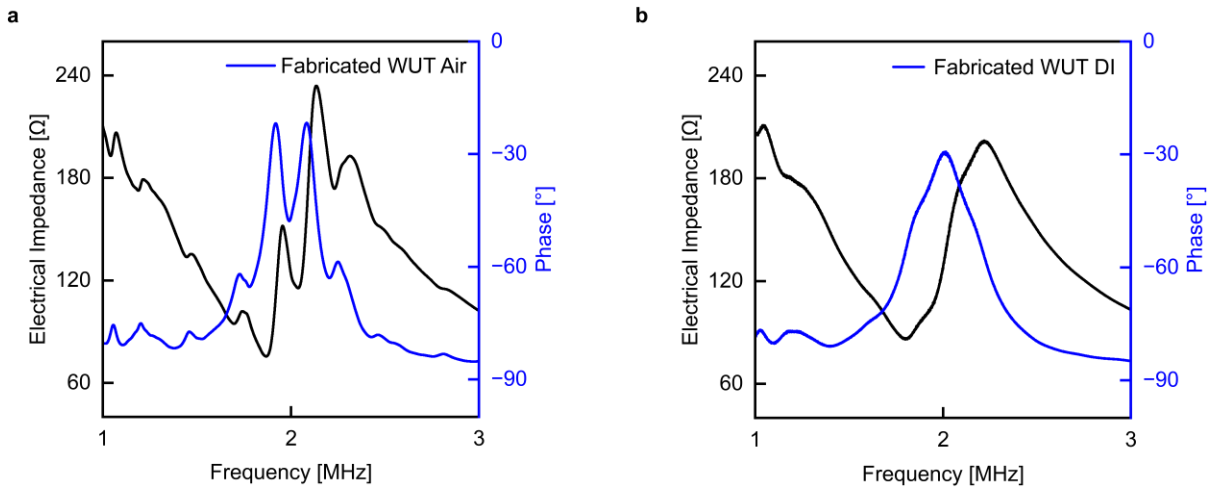

Supplementary Fig. 6: Electrical impedance magnitude and phase response of the WUT after matching and backing layer (BL) coating (Fabricated WUT). a, b, Frequency sweep results of the ML-BL-coated wearable ultrasound transducer from 1 MHz to 3 MHz in air **(a)** and in DI water **(b)**.

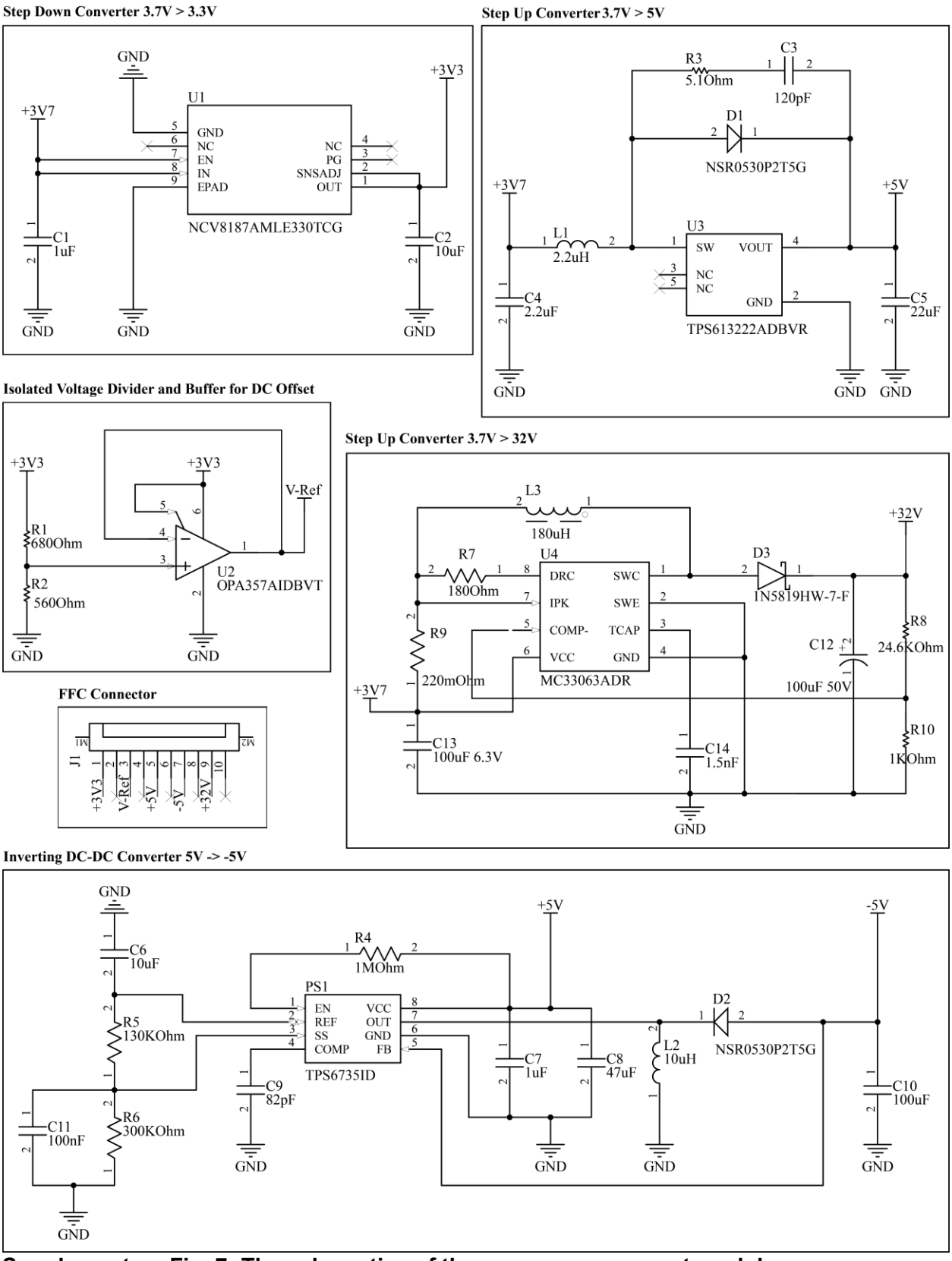

Supplementary Fig. 7: The schematics of the power management module.

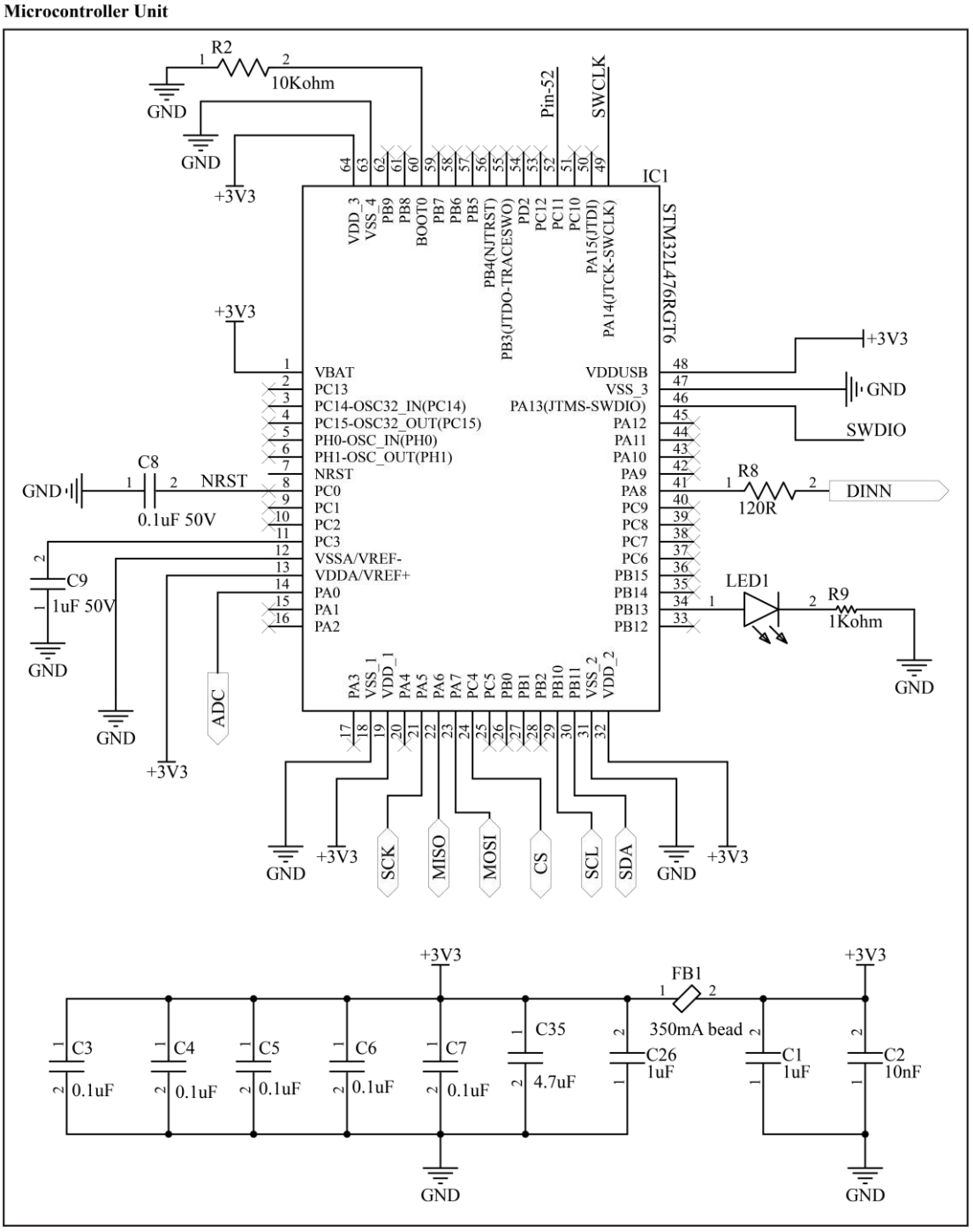

Supplementary Fig. 8: The schematics of the microcontroller unit.

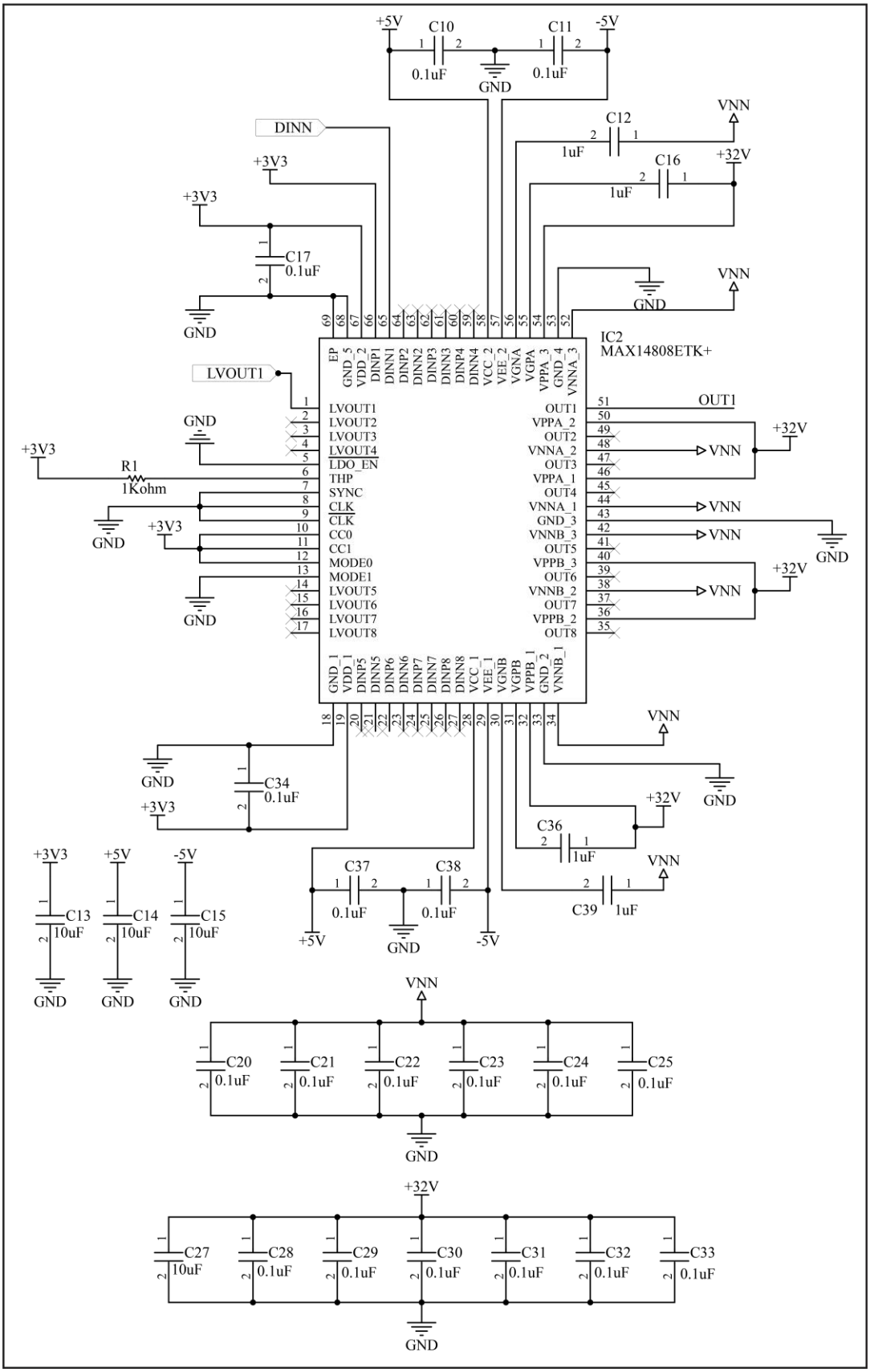

Supplementary Fig. 9: The schematics of the high-voltage pulser unit.

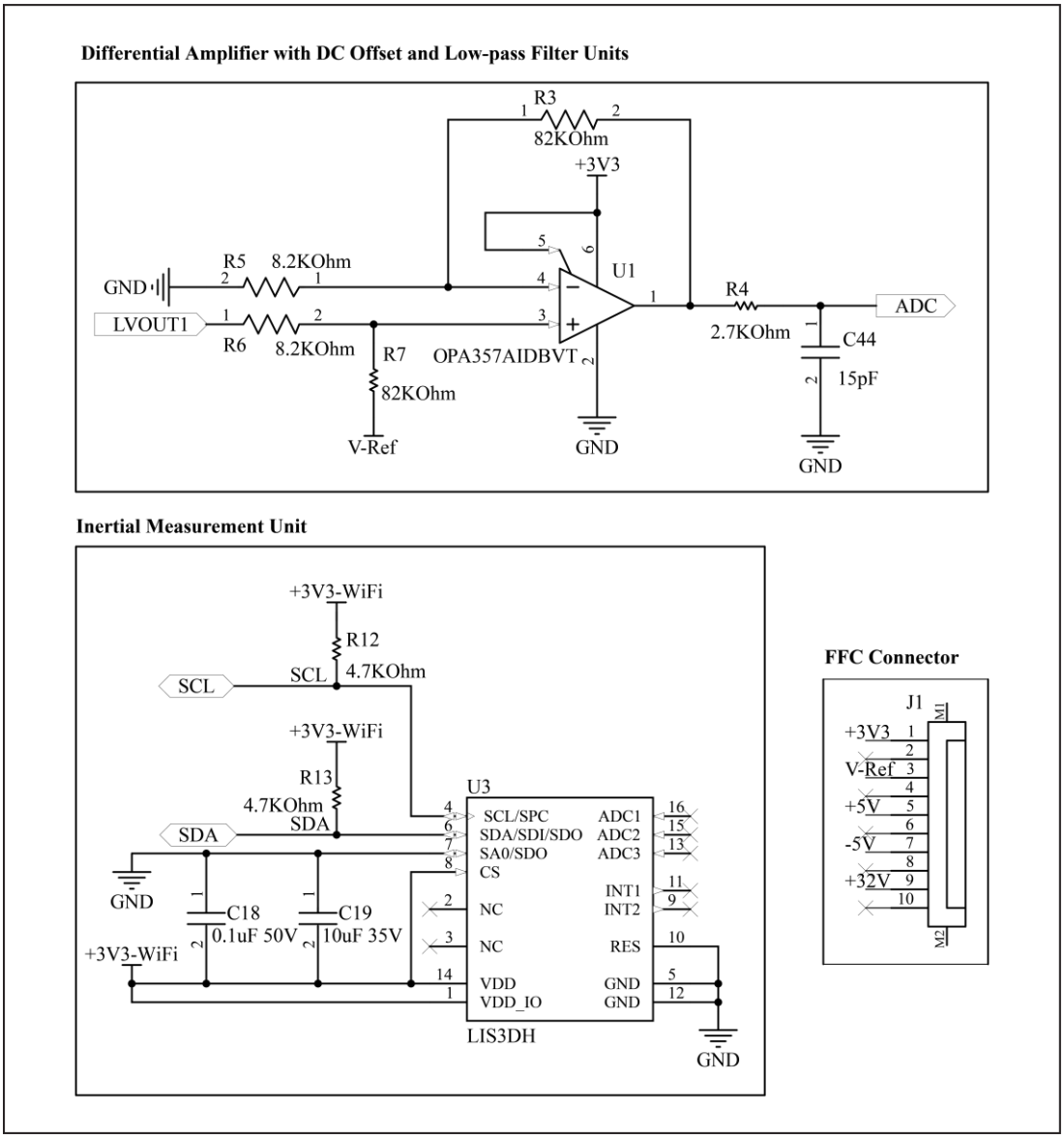

Supplementary Fig. 10: The schematics of the differential amplifier with DC offset, low-pass filter and IMU units.

Wi-fi Unit

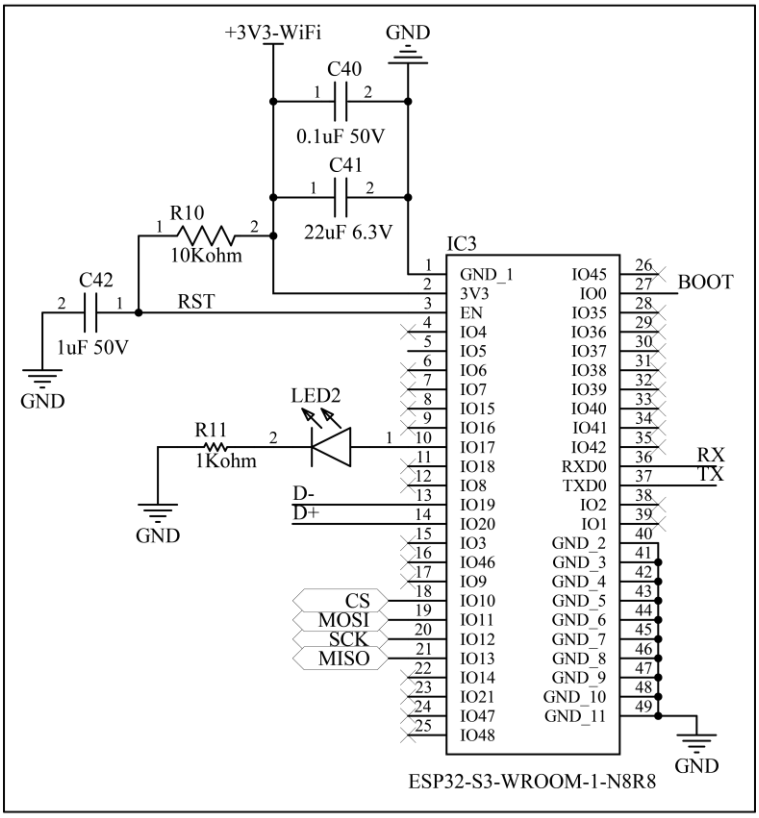

Step Down Converter 3.7V > 3.3V

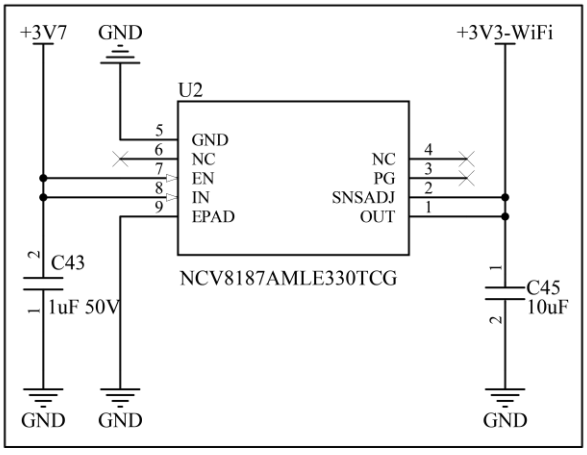

Supplementary Fig. 11: The schematics of the Wi-Fi unit with and LDO regulator.

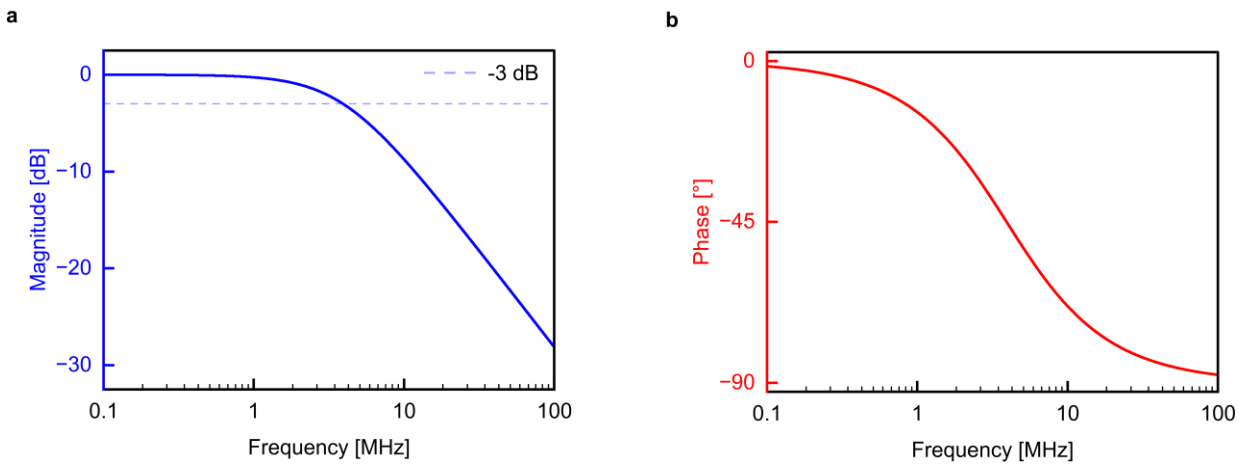

Supplementary Fig. 12: Bode response of the RC low-pass filter. a, Magnitude response of the RC low-pass filter with -3 dB reference indicated. **b,** Phase response of the RC low-pass filter.

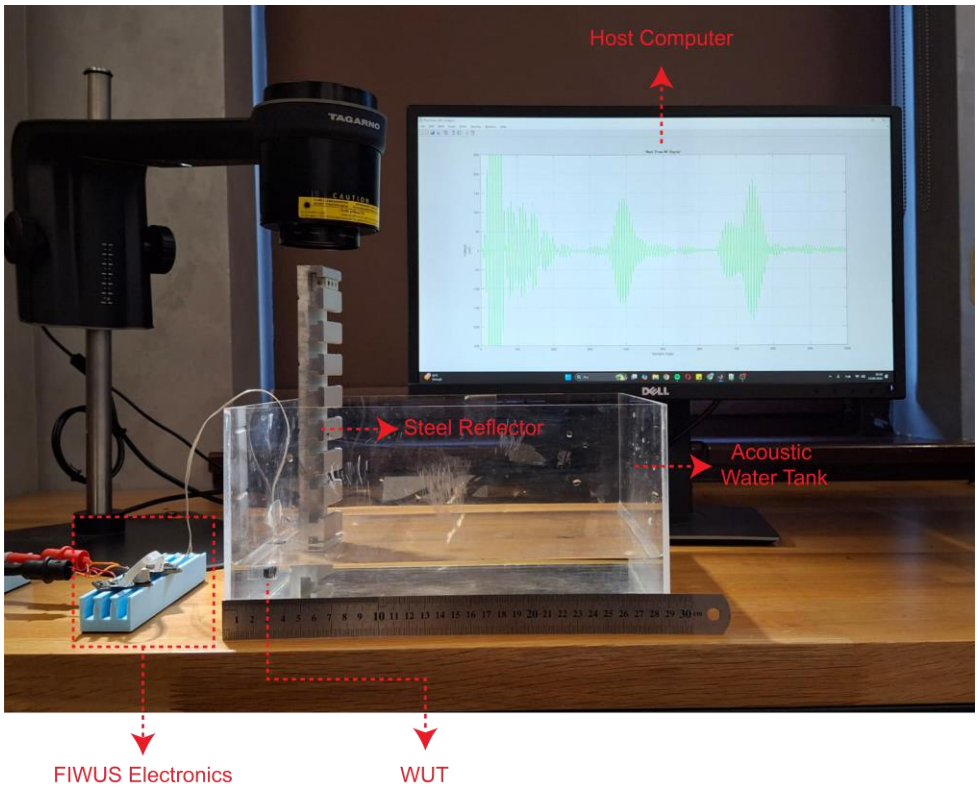

Supplementary Fig. 13: Pulse-echo experiment setup for real-time wireless ultrasound data transmission.

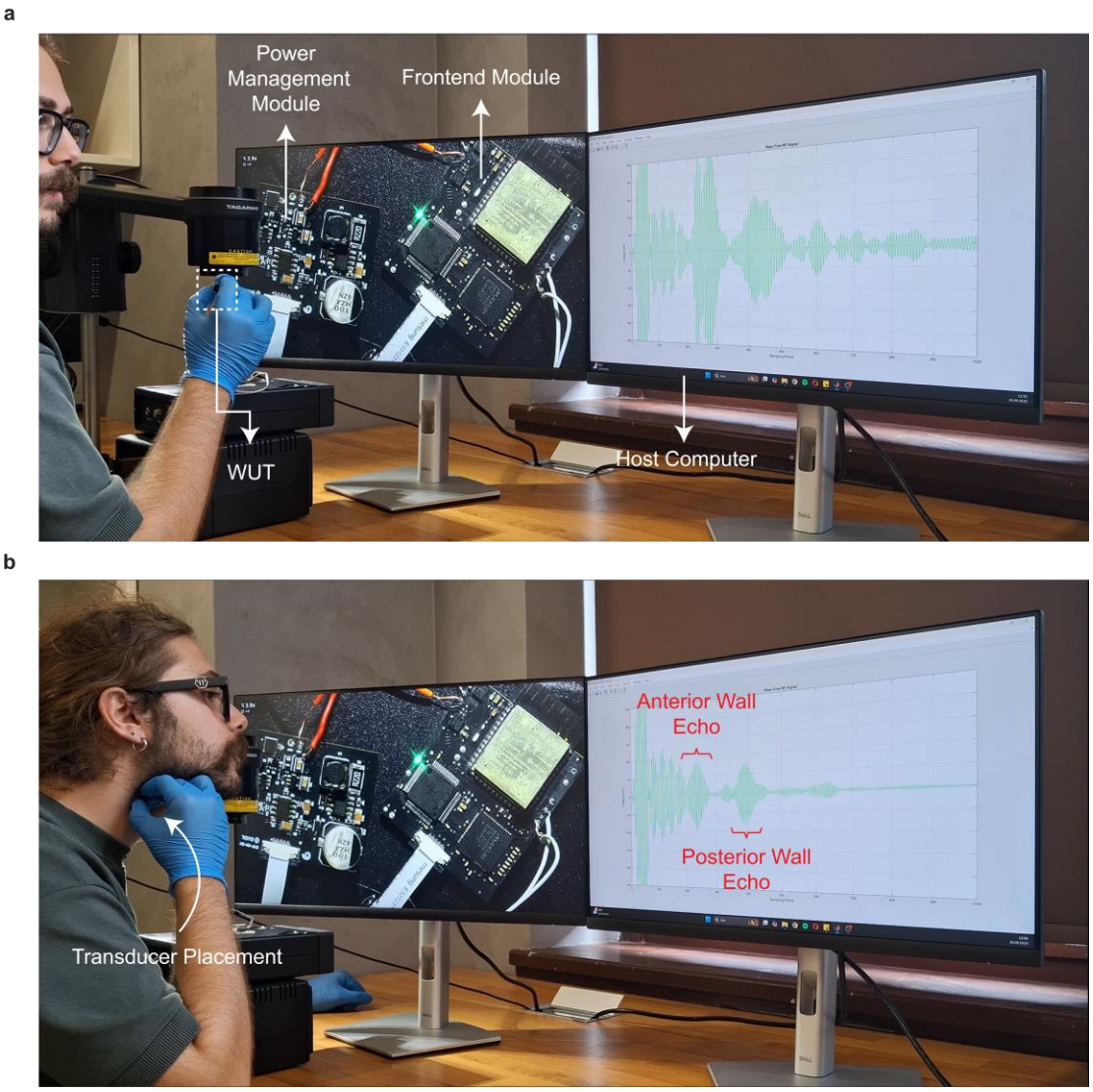

Supplementary Fig. 14: In-vivo validation of the FIWUS. a, Experimental setup showing the WUT placed on the subject's neck and wirelessly interfaced with the power management and frontend modules. The acquired echo signals are transmitted to the host computer for real-time data acquisition. **b,** Placement of the WUT on the carotid artery with corresponding ultrasound A-mode signals. The anterior and posterior arterial wall echoes are identified, which are subsequently tracked to derive pulsatile vessel motion and blood pressure waveforms.

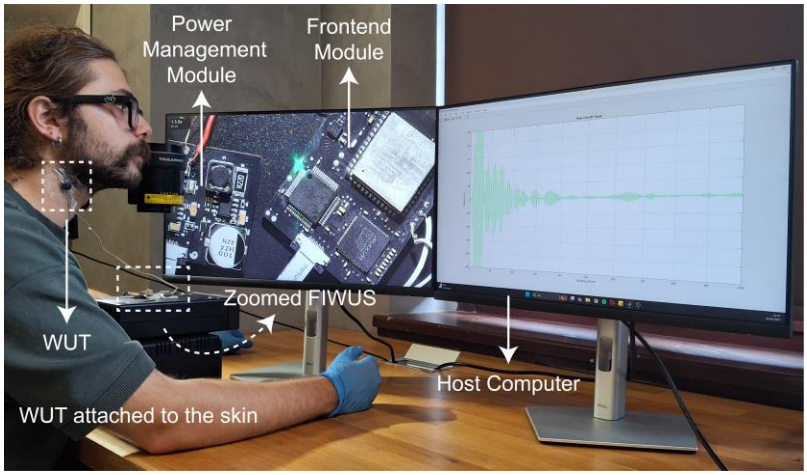

Supplementary Fig. 15: System-level demonstration of the FIWUS. The wearable ultrasound transducer is attached to the skin using medical double-sided tape to ensure stable coupling during in-vivo measurements. The transducer is wirelessly interfaced with the power management and frontend modules, enabling excitation and signal acquisition. A zoomed view of the FIWUS electronics is displayed on the left monitor, while the received echo signals are visualized in real time on the host computer.

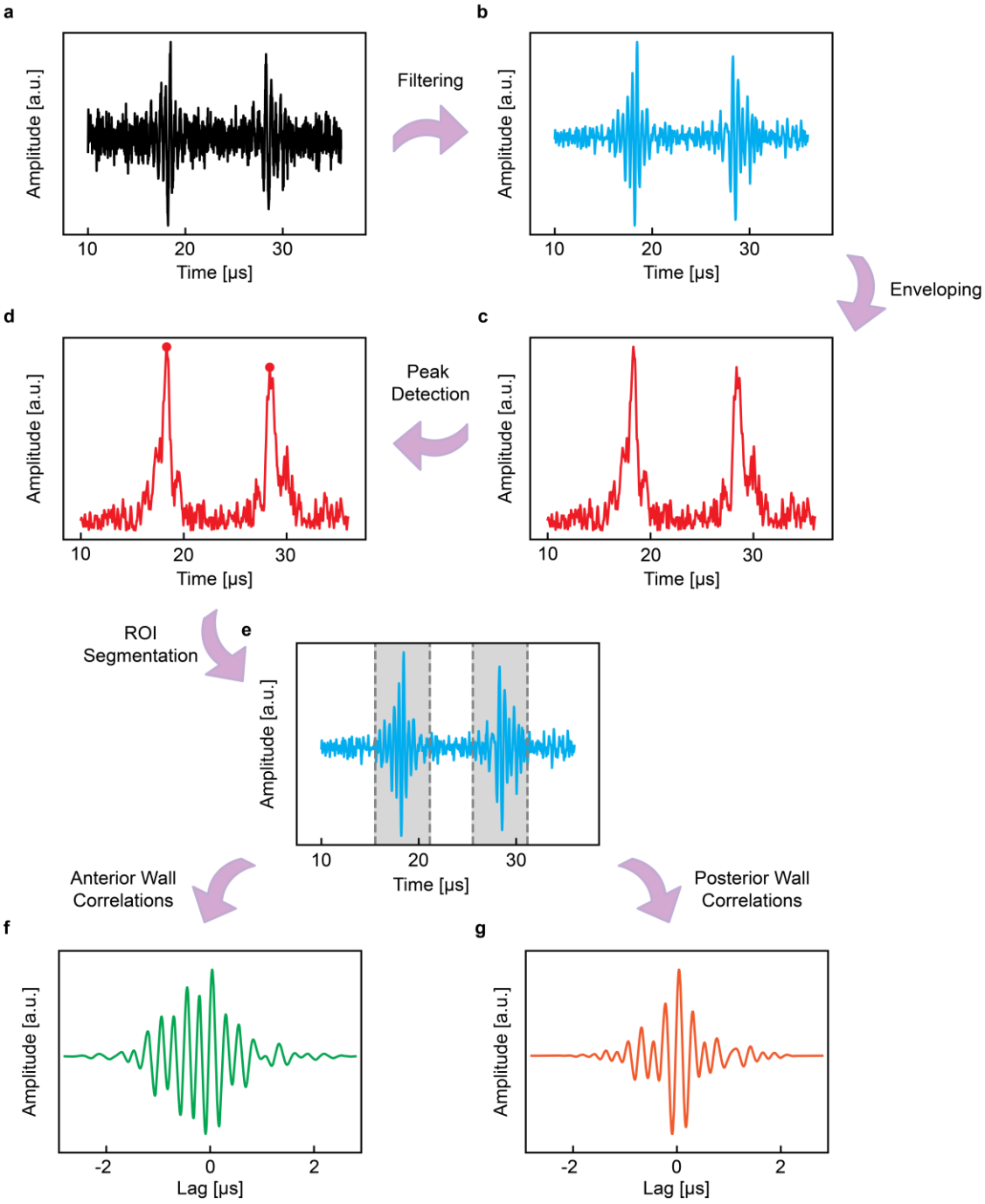

Supplementary Fig. 16: Signal processing algorithm for blood pressure monitoring. a, Raw ultrasound RF signal acquired from the wearable ultrasound transducer. **b,** Bandpass filtering of the RF signal to isolate the vessel wall echoes. **c,** Envelope detection applied to highlight echo peaks. **d,** Identification of the anterior and posterior wall echo peaks. **e,** Segmentation of regions of interest (ROIs) around the detected peaks. **f, g,** Correlation of segmented ROIs across successive frames to track anterior **(f)** and posterior **(g)** wall displacements.

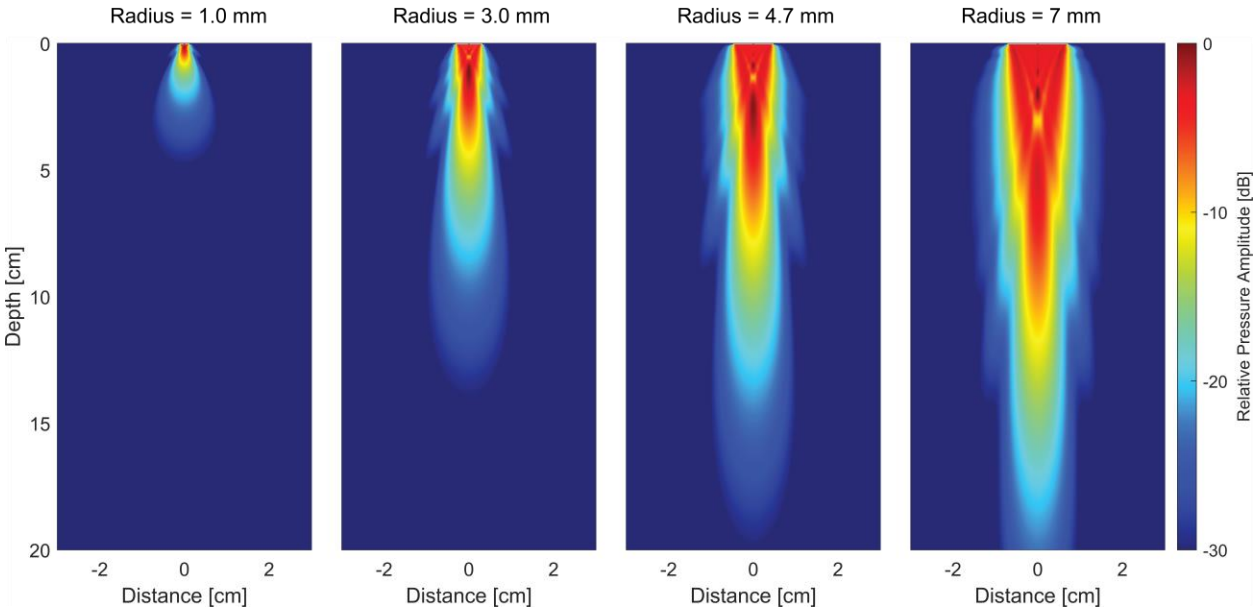

Supplementary Fig. 17: Longitudinal acoustic pressure field simulations of disc-shaped ultrasound transducers with radii of 1.0, 3.0, 4.7, and 7.0 mm.

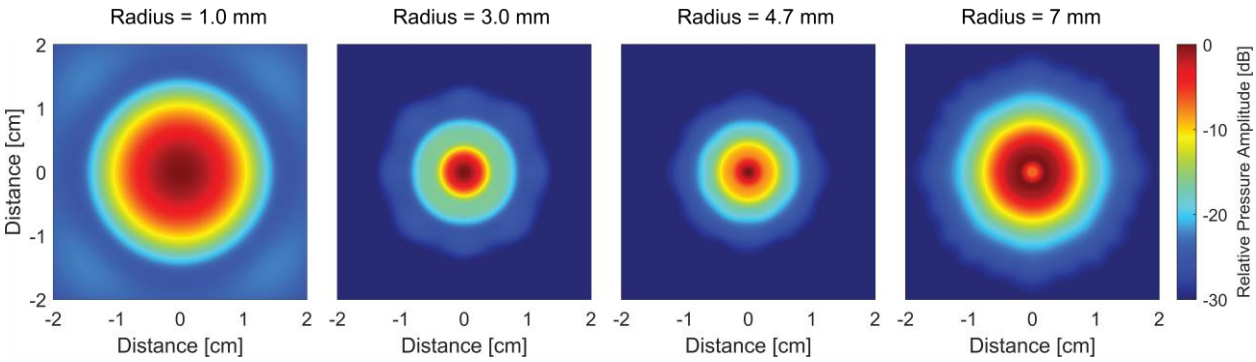

Supplementary Fig. 18: Transverse acoustic pressure field simulations of disc-shaped ultrasound transducers with radii of 1.0, 3.0, 4.7, and 7.0 mm.

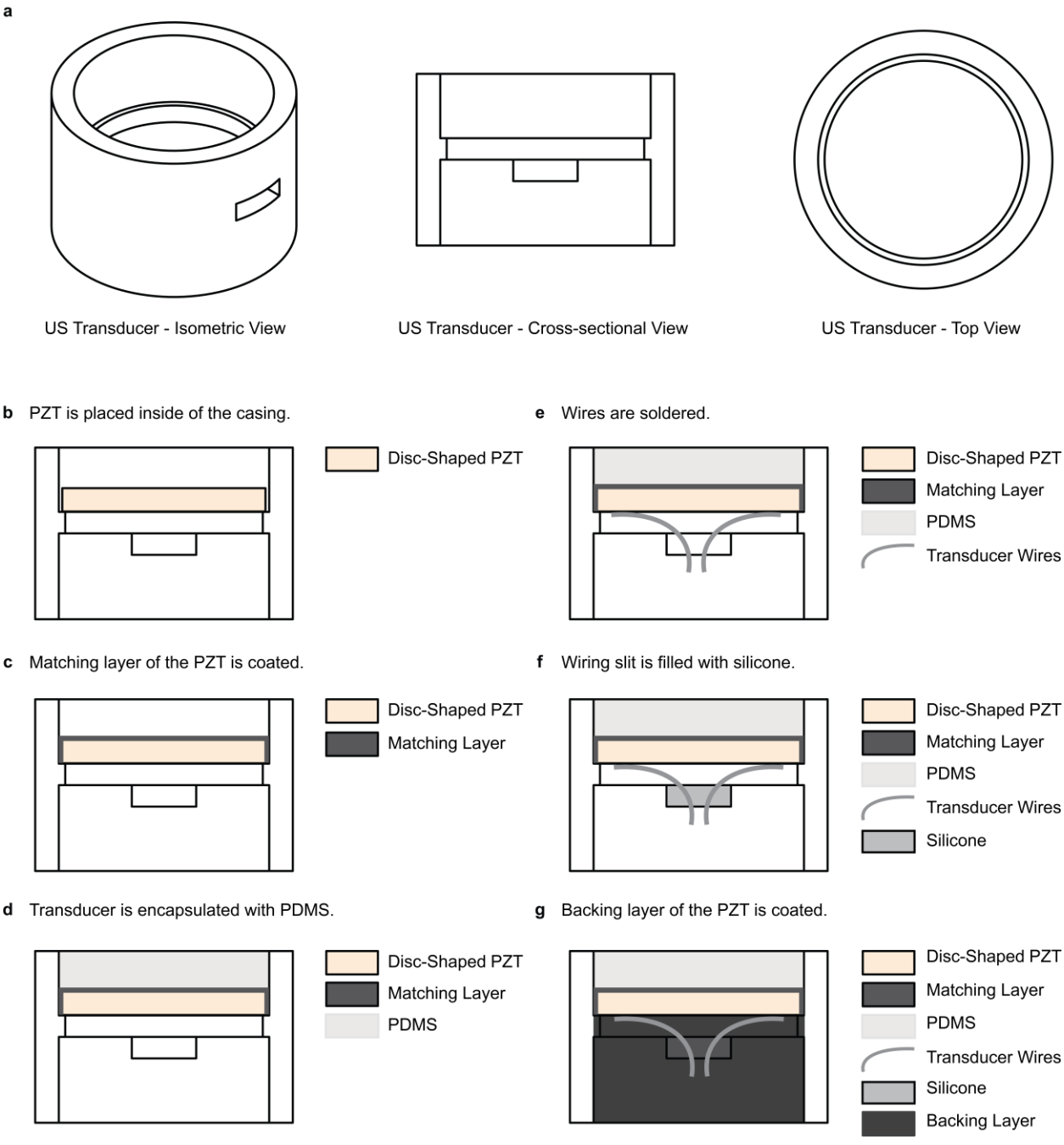

Supplementary Fig. 19: Schematic illustration of the WUT fabrication workflow. a, Schematic illustrations of the WUT clear resin housing. **b,** PZT placement into to the casing. **c,** Matching layer coating of the WUT. **d,** Encapsulation of the WUT with PDMS. **e,** Wire bonding of the WUT. **f,** Filling the wiring slit with silicone. **g,** Backing layer coating of the WUT.

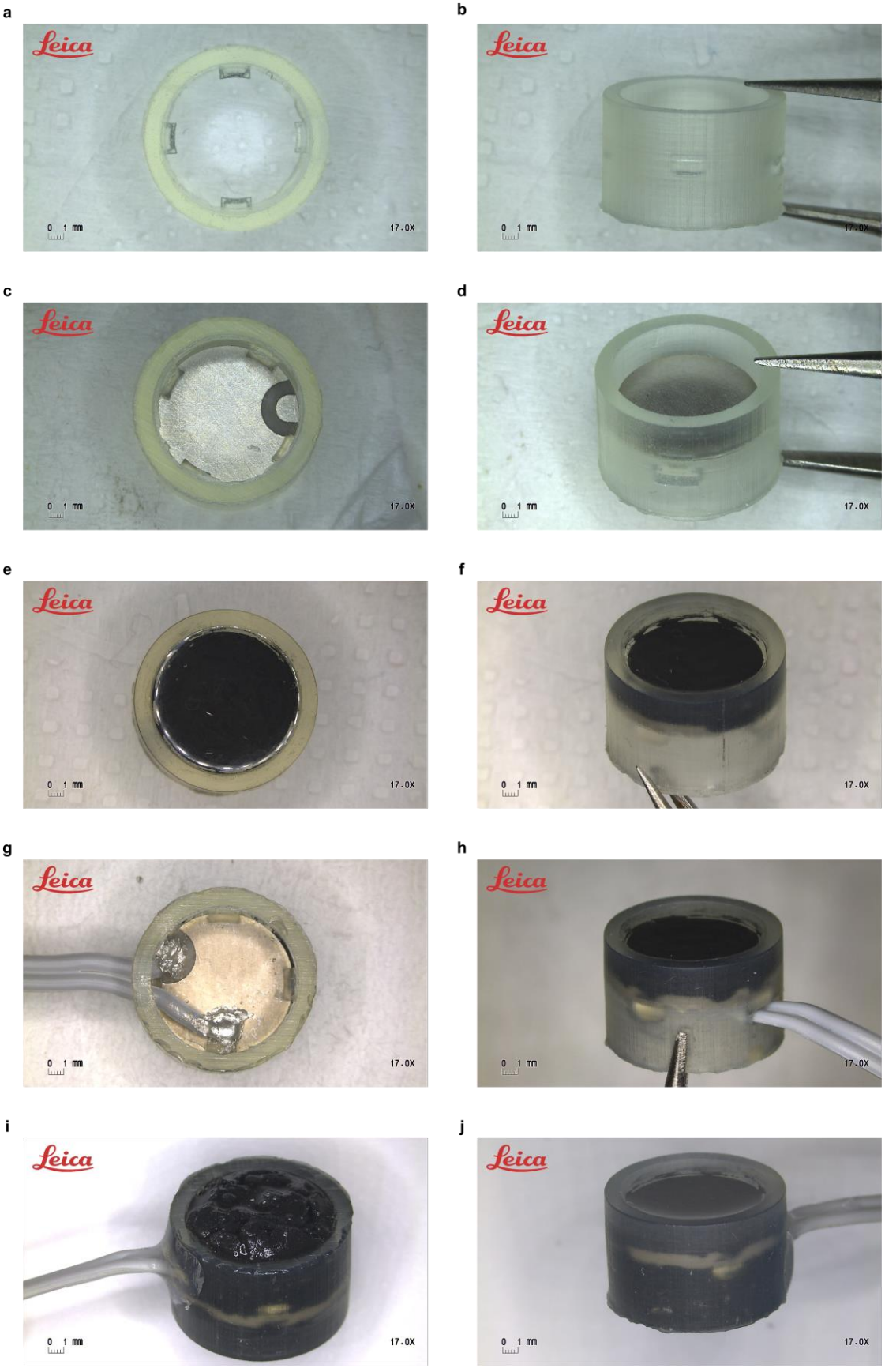
a
b
c
d
e
f
g
h
i
j
Leica
0 1 mm
17.0X

Supplementary Fig. 20: Fabrication of the wearable ultrasound transducer. a, b, Top view **(a)** and side view **(b)** of the mechanical casing for the wearable ultrasound transducer. **c, d,** Placement of the disc PZT inside the mechanical casing bottom view **(c)** and oblique view **(d)**. **e, f,** Matching layer coating and PDMS encapsulation of the WUT top view **(e)** and side view **(f)**. **g, h,** Electrical connections of the PZT with conductive silver-epoxy bottom view **(g)** and oblique view **(h)**. **i, j,** Backing layer coated wearable ultrasound transducer top view **(i)** and oblique view **(j)**.

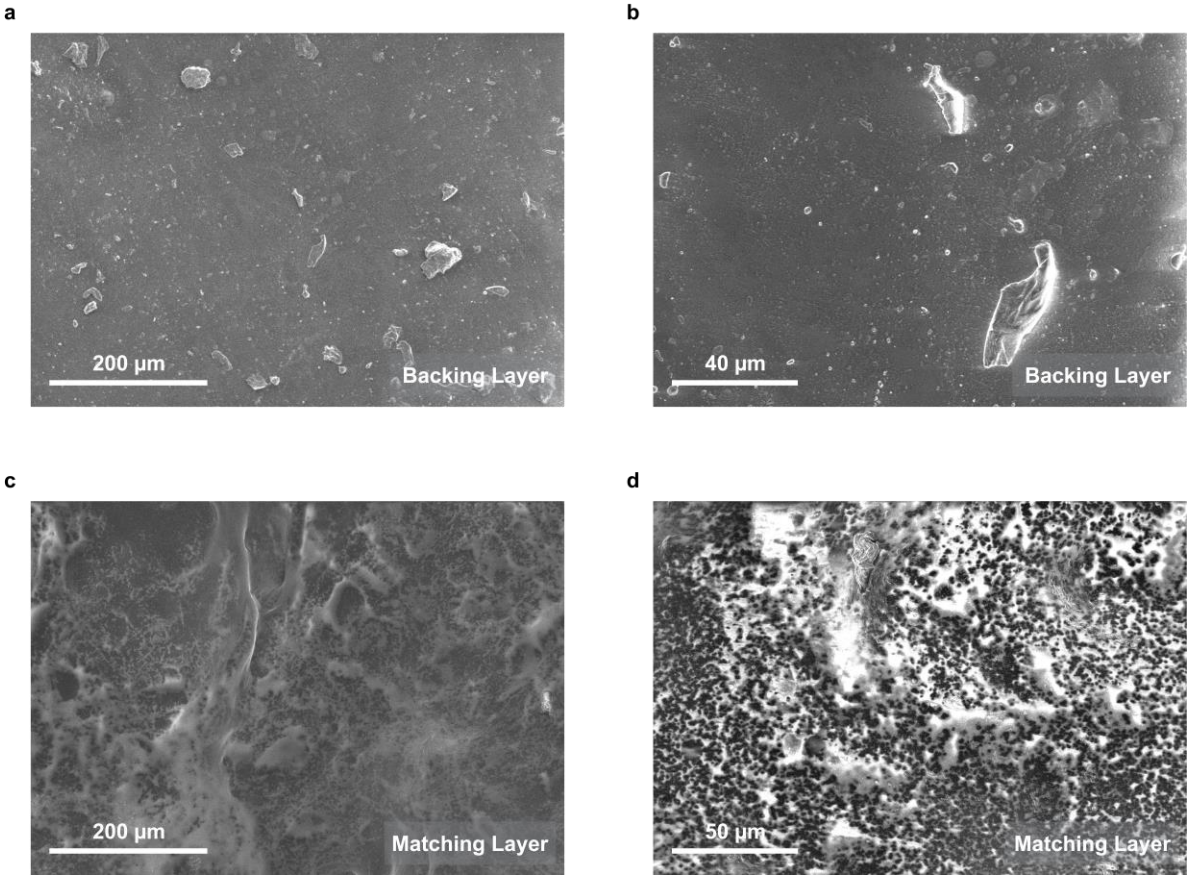

Supplementary Fig. 21: Scanning electron microscope (SEM) images of the acoustic backing and matching layers of the WUT. a,b, SEM micrographs of the backing layer at different magnifications. **c,d,** SEM micrographs of the matching layer at different magnifications.

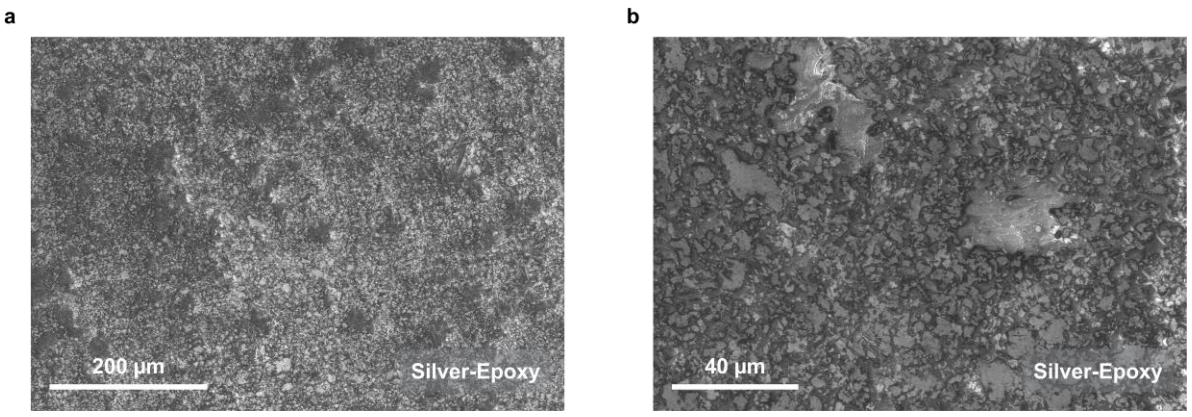

Supplementary Fig. 22: SEM images of the silver-epoxy of the WUT. a,b, SEM micrographs of the conductive silver-epoxy at different magnifications.

Supplementary Table 1. Average current consumption of the fully integrated wearable ultrasound system.

Component	Quantity	Average Current Consumption
MCU	1	16mA
HV Pulser	1	20mA
Wi-Fi	1	105mA
Op-amp	2	4.9mA
IMU	1	225μA
LDO Regulator	2	30μA
Boost Converter (5V)	1	6.5μA
Boost Converter (32V)	1	4mA
Inverting Converter	1	1.9mA

Supplementary Video 1. FIWUS device operation and pulse-echo experiments. The FIWUS wirelessly transmits the ultrasound signals to the host computer in real-time, and the received echo signals are monitored in the host computer screen. The WUT and steel reflector were placed inside of the acoustic water tank, and echo signals scattered from the steel reflector were acquired at various distances.

Supplementary Video 2. Autonomous monitoring the pulsatile movement of the carotid artery and tracking the arterial walls in real-time. The WUT was placed on the neck of the subject and aligned to the CCA. The pulsatile movement of the anterior and posterior walls of the CCA was monitored.

References

1. Jensen, J. A. & Svendsen, N. B. Calculation of pressure fields from arbitrarily shaped, apodized, and excited ultrasound transducers. *IEEE Trans Ultrason Ferroelectr Freq Control* **39**, 262–267 (1992).

2. Jensen, J. FIELD: A program for simulating ultrasound systems. *Med Biol Eng Comput* **34**, 351–352 (1996).

3. Patterson, B. & Miller, D. L. Experimental Measurements of Ultrasound Attenuation in Human Chest Wall and Assessment of the Mechanical Index for Lung Ultrasound. *Ultrasound Med Biol* **46**, 1442–1454 (2020).

4. Fan, W. *et al.* Analysis of the anatomic eligibility for transcarotid artery revascularization in Chinese patients who underwent carotid endarterectomy and transfemoral carotid artery stenting. *Front Cardiovasc Med* **Volume 9-2022**, (2023).

5. Leach, W. M. Controlled-source analogous circuits and SPICE models for piezoelectric transducers. *IEEE Trans Ultrason Ferroelectr Freq Control* **41**, 60–66 (1994).

6. van Deventer, J., Lofqvist, T. & Delsing, J. PSpice simulation of ultrasonic systems. *IEEE Trans Ultrason Ferroelectr Freq Control* **47**, 1014–1024 (2000).

7. Shen, Z. *et al.* An Improved Equivalent Circuit Simulation of High Frequency Ultrasound Transducer. *Front Mater* **Volume 8-2021**, (2021).

8. Saul, T. *et al.* M-Mode Ultrasound Applications for the Emergency Medicine Physician. *J Emerg Med* **49**, 686–692 (2015).

9. Li, J., Zhu, K. & Pan, L. Wrist and finger motion recognition via M-mode ultrasound signal: A feasibility study. *Biomed Signal Process Control* **71**, 103112 (2022).

10. Stadler, R. W., Andrew Taylor, J. & Lees, R. S. Comparison of B-mode, M-mode and echo-tracking methods for measurement of the arterial distension waveform. *Ultrasound Med Biol* **23**, 879–887 (1997).

11. Bunce, S. M., Hough, A. D. & Moore, A. P. Measurement of abdominal muscle thickness using M-mode ultrasound imaging during functional activities. *Man Ther* **9**, 41–44 (2004).